

## Supplementary Information

### Work function-tailored graphene *via* transition metal encapsulation as a highly active and durable catalyst for the oxygen reduction reaction

Monika Sharma,<sup>‡*a*</sup> Jue-Hyuk Jang,<sup>‡*bc*</sup> Dong Yun Shin,<sup>*d*</sup> Jeong An Kwon,<sup>*d*</sup> Dong-Hee Lim,<sup>*d*</sup> Daeil Choi,<sup>*be*</sup> Hukwang Sung,<sup>*a*</sup> Jeonghee Jang,<sup>*a*</sup> Sang-Young Lee,<sup>*f*</sup> Kwan Young Lee,<sup>*c*</sup> Hee-Young Park,<sup>*b*</sup> Namgee Jung,<sup>\**a*</sup> and Sung Jong Yoo<sup>\**beg*</sup>

<sup>*a*</sup> Graduate School of Energy Science and Technology (GEST), Chungnam National University, Daejeon 34134, Republic of Korea.

<sup>*b*</sup> Center for Hydrogen Fuel Cell Research, Korea Institute of Science and Technology (KIST), Seoul 02792, Republic of Korea.

<sup>*c*</sup> KU-KIST Green School, Graduate School of Energy and Environment, Korea University, Seoul 02841, Republic of Korea.

<sup>*d*</sup> Department of Environmental Engineering, Chungbuk National University, Cheongju, Chungbuk 28644, Republic of Korea.

<sup>*e*</sup> Division of Energy & Environment Technology, KIST School, University of Science and Technology (UST), Seoul 02792, Republic of Korea.

<sup>*f*</sup> Research Division, Environmental Technology Institute, COWAY, Seoul 08826, Republic of Korea.

<sup>*g*</sup> KHU-KIST Department of Converging Science and Technology, Kyung Hee University, Seoul 02447, Republic of Korea.

### Corresponding Authors

njung@cnu.ac.kr (N. Jung), ysj@kist.re.kr (S. J. Yoo)

<sup>‡</sup> These authors have contributed equally.

## **SI 1. Material Characterization:**

### **(a) XRD Results:**

Fig. S1 represents XRD patterns of as-synthesized and annealed samples in comparison of commercial Co/C catalyst (20 wt.%, Premetek). Although the background noise level is high due to the significant Co fluorescence but the diffraction peaks corresponding to various components are properly resolved. The XRD pattern of all samples show a broad peak, centred at around  $25^\circ$  ( $2\theta$ ) which corresponds to (002) plane of amorphous carbon support. The Co@G/C\_ ASP sample exhibit a multiphase structure consisting of metallic cobalt and cobalt oxides. The peak positions of metallic cobalt are slightly shifted to a lower angle in contrast to the pure metallic cobalt and slightly towards cobalt carbide  $\text{CoC}_x$  peak position. Based on the XRD pattern, it is difficult to differentiate between metallic cobalt and cobalt carbide due to their similar XRD peak positions, but lower angle shift in metallic cobalt peak position can be explained by the dissolution of some carbon atoms into the cobalt nanoparticles or by only partial mixing between C and Co states. In other words, here, the estimated lattice parameter (a,b) increased from  $2.506 \text{ \AA}$  to  $2.622 \text{ \AA}$  for cobalt. This lattice distortion in the cobalt crystal lattice or lattice expansion confirms the incorporation of carbon atom into crystal lattice of cobalt<sup>1-3</sup>. The extra peaks observed at  $2\theta$  values of 36.5, 42.4, and 61.6 are assigned to scattering from the (111), (200), and (220) planes, respectively, of the CoO (JCPDS File Card No.-78-0431)<sup>4-6</sup> while diffraction peaks at 36.79 and 44.8 corresponding to (200) and (222) planes, respectively, are of cubic  $\text{Co}_3\text{O}_4$  phase and matches well with JCPDS File Card No.-78-1969.<sup>7-9</sup> Hence, XRD results of Co@G/C\_ ASP confirm that the presence of both CoO and  $\text{Co}_3\text{O}_4$ . The XRD pattern of Co@G/C\_500 sample shows metallic cobalt along with a very weak peak for  $\text{Co}_3\text{O}_4$  phase while no peaks corresponding to the phases of cobalt oxides were detected in Co@G/C\_600 and Co@G/C\_700 samples, indicating that these heat-treated nanoparticles have only pure metallic cobalt phase. In our samples, two phases of cobalt- face centered-cubic (fcc) and hexagonal close-packed (hcp) coexist with fcc as the predominant phase. The major diffraction peaks at  $2\theta$  values of  $44.35^\circ$  and  $75.95^\circ$  corresponding to (111) and (220) crystal planes, respectively, can be indexed as fcc-phase metallic cobalt (JCPDS File Card No. 15-0806,  $a = 3.5447 \text{ \AA}$ ).<sup>10</sup> Moreover, hcp-phase cobalt could also be detected as peaks corresponding to 41.6, 44.5, 47.6 and 75.8 related to (100), (002), (101) and (110) planes, respectively, (JCPDS File Card No. 01-071-4239,  $a = 2.506 \text{ \AA}$ ,  $c = 4.069 \text{ \AA}$ ).<sup>11</sup> In literature, there are several reports which mention the synthesis of cobalt nanostructures having two

phases together.<sup>12,13</sup> For all the samples, the weak peaks in the XRD patterns may be caused due to small size ( $\leq 5$  nm) and low crystallinity of the nanoparticles.

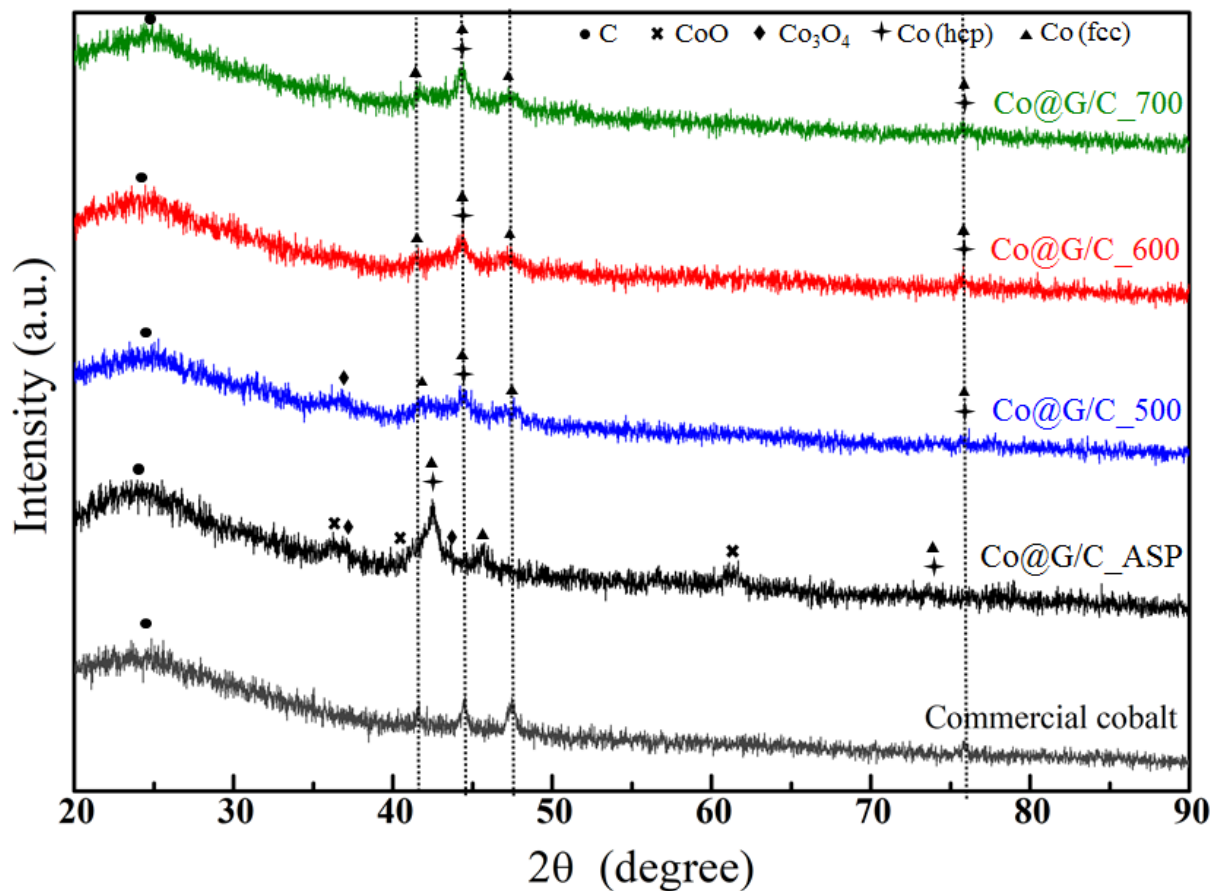


**Fig. S1.** XRD patterns of 20 wt.% commercial cobalt catalyst (Pemetek), Co@G/C\_ASP, Co@G/C\_500, Co@G/C\_600, and Co@G/C\_700.

**(b) XPS Results:**

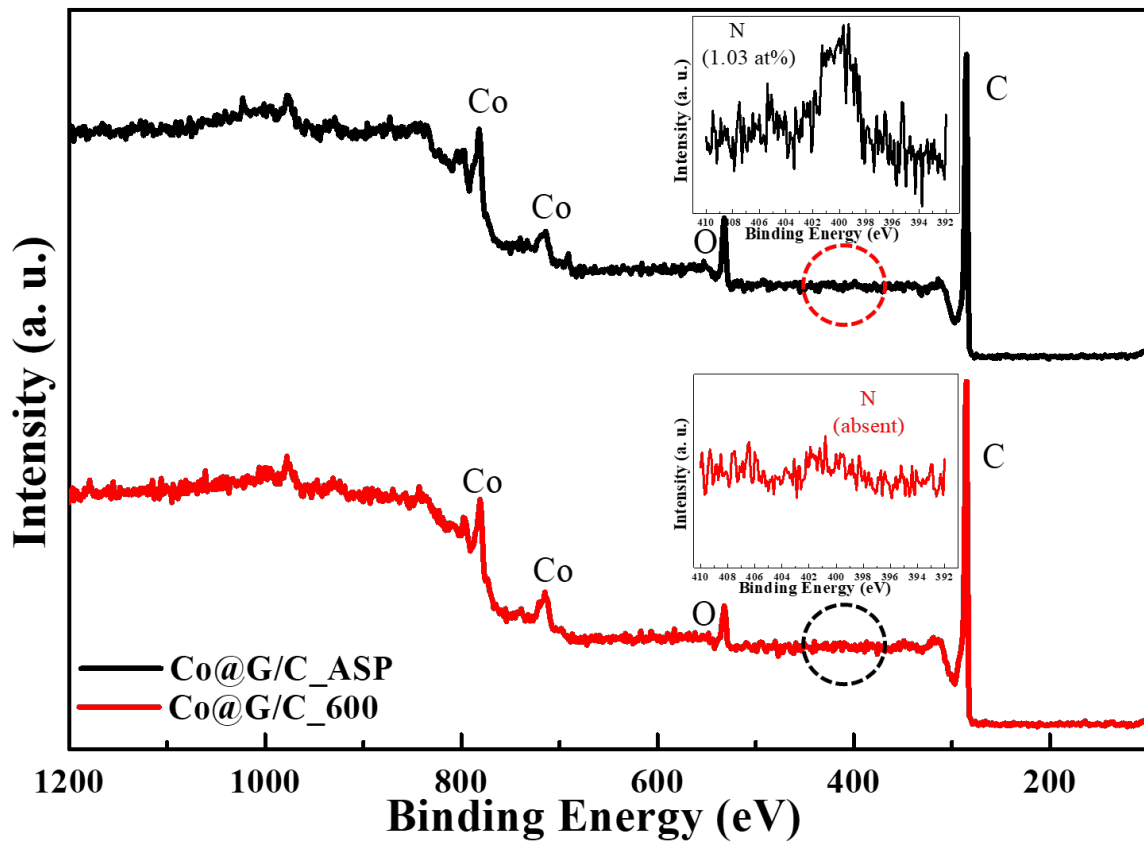


**Fig. S2.** XPS survey scan of Co@G/C\_ASP, and Co@G/C\_600. Inset shows N 1s spectrum.

**(c) TEM Results:**

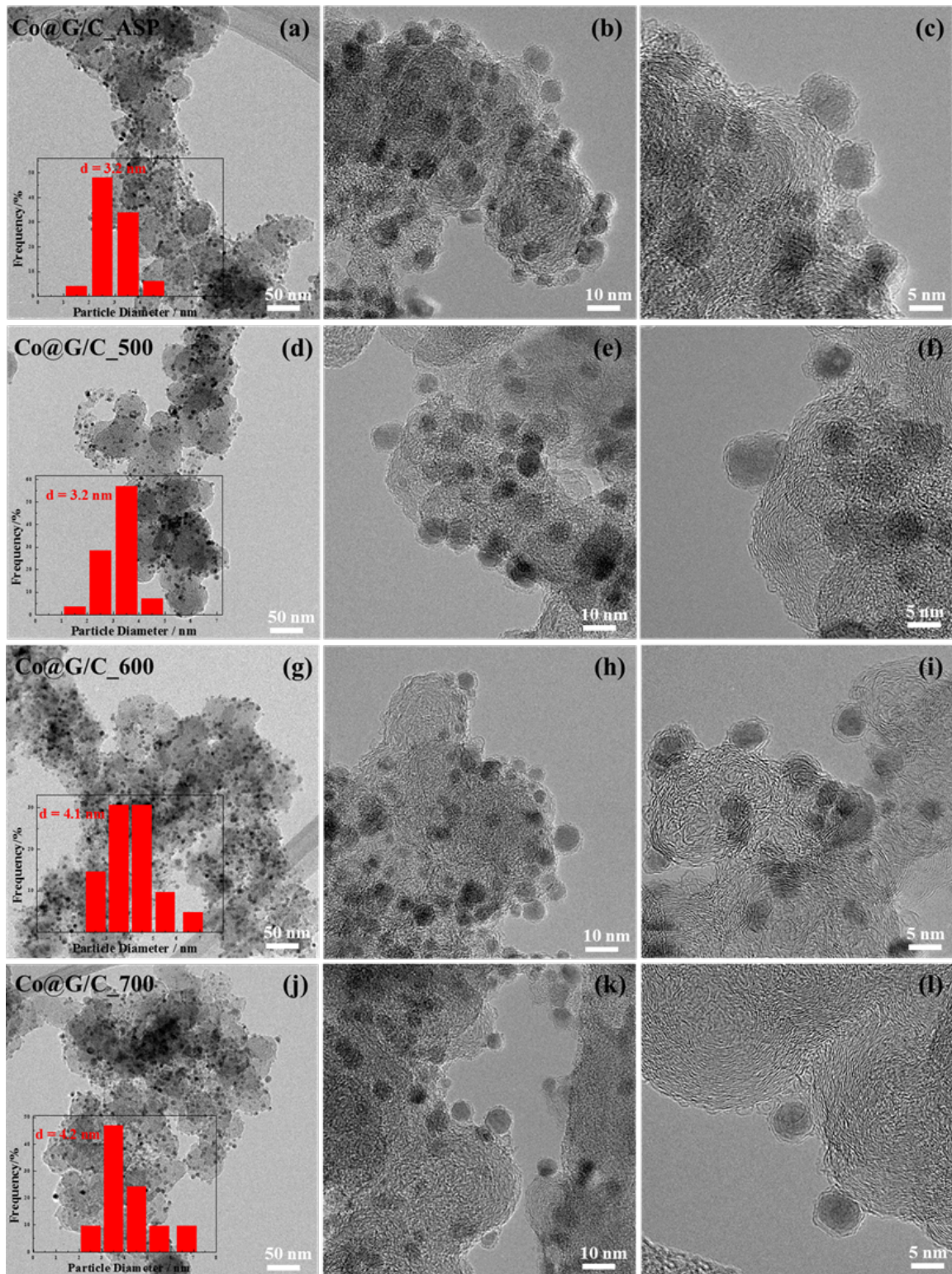


**Fig. S3.** Transmission electron microscope (TEM) images of **(a-c)** Co@G/C\_700, **(d-f)** Co@G/C\_600, **(g-i)** Co@G/C\_500, and **(j-l)** Co@G/C\_700 at different magnifications. Inset shows corresponding particle size distribution histograms.

For more detailed structure analysis, Co@G/C<sub>ASP</sub> and Co@G/C<sub>600</sub> were further examined by high-resolution TEM (HR-TEM). HRTM images of Co@G/C<sub>600</sub> (Fig. S4 (c,d)) reveal that the lattice fringes of the encapsulated nanoparticles have interplanar spacing of 0.204 nm which is ascribed to (111) plane of the fcc-metallic cobalt, respectively.<sup>14-17</sup> Moreover, graphitic layers having distinct lattice fringes with *d*-spacing of about 0.34 nm. enfold completely the metal particles and are of crystalline nature.

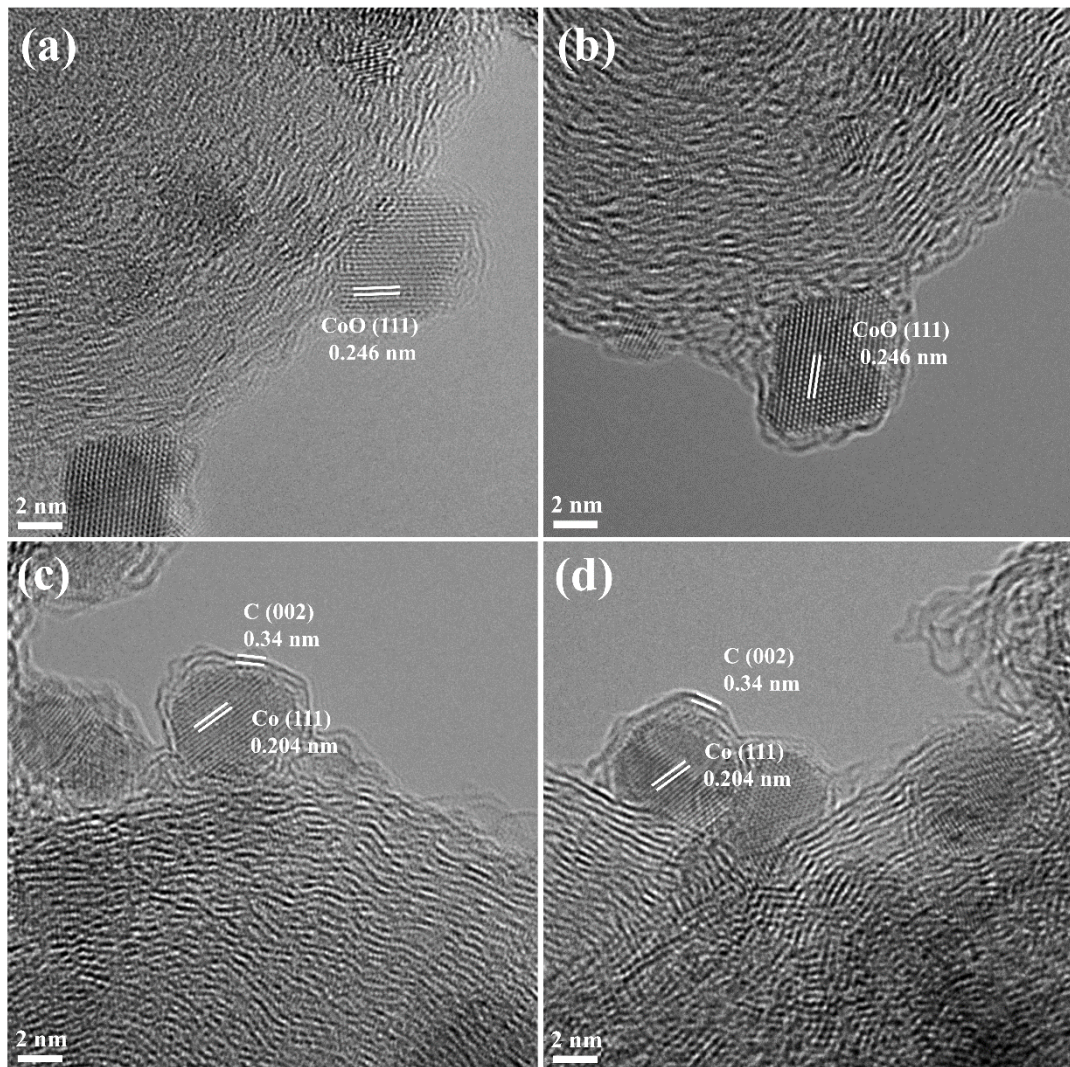


**Fig. S4.** HR-TEM images of Co@G/C<sub>ASP</sub> (**a,b**) and Co@G/C<sub>600</sub> (**c,d**).

## SI 2. Electrochemical Characterization:

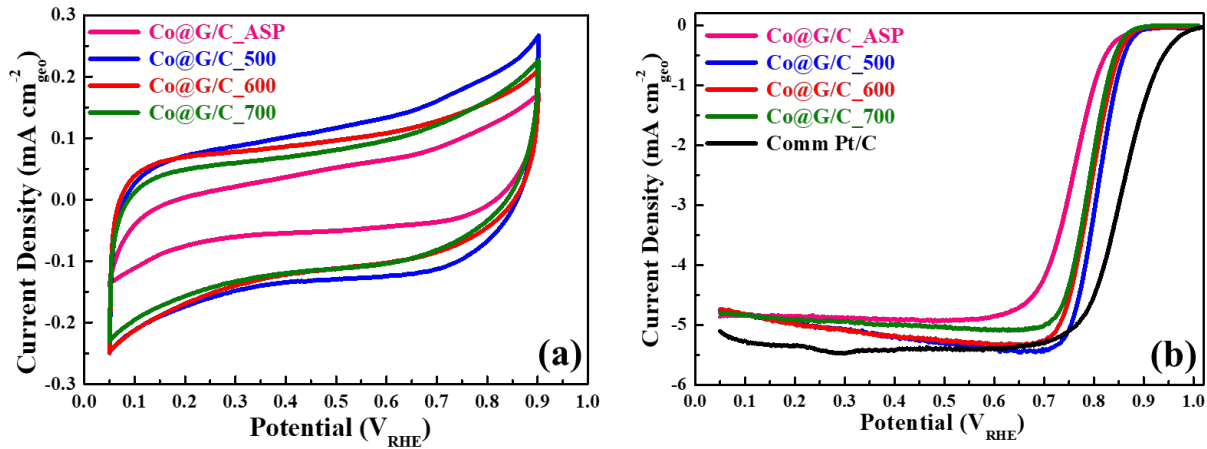


**Fig. S5.** (a) CV and (b) ORR polarization results of Co@G/C<sub>ASP</sub>, Co@G/C<sub>500</sub>, Co@G/C<sub>600</sub> and Co@G/C<sub>700</sub> in 0.1 M KOH. For CVs, scan rate: 20 mV s<sup>-1</sup>, Ar-saturated, For ORRs, scan rate: 5 mV s<sup>-1</sup>, rotation rate: 1600 rpm, O<sub>2</sub>-saturated.

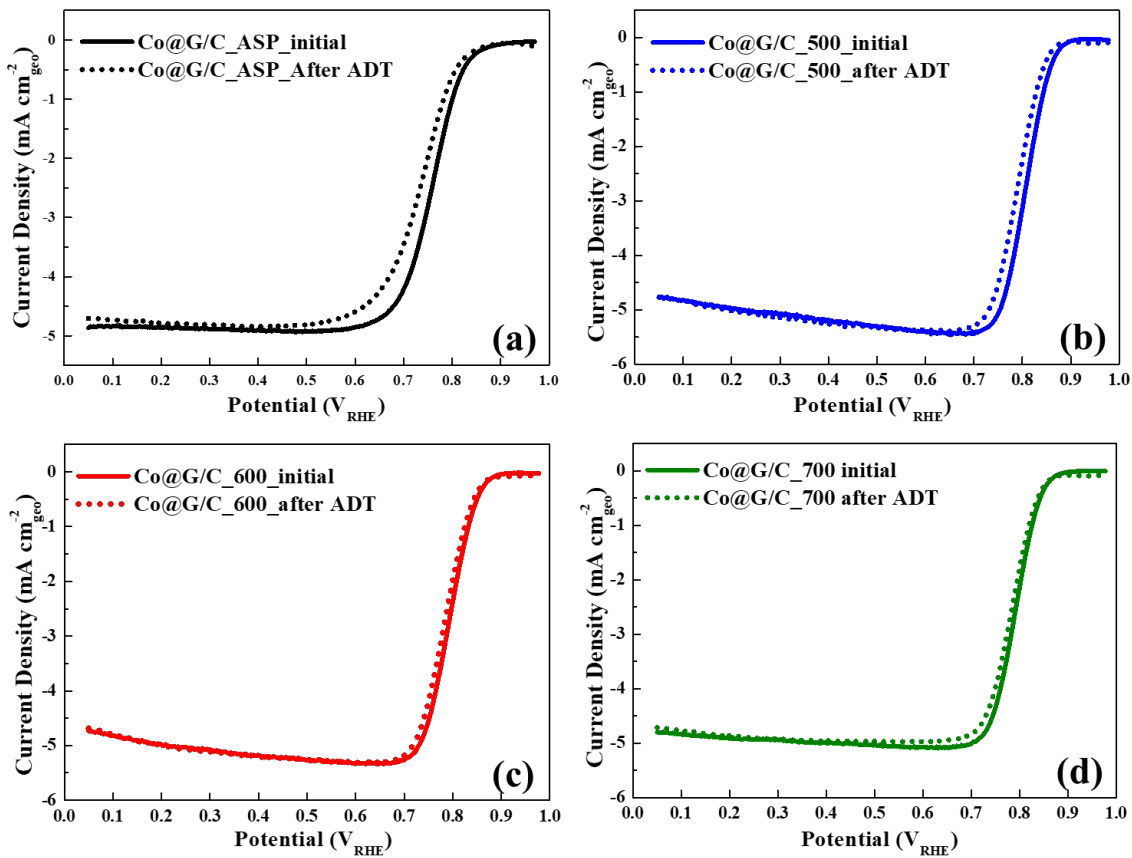


**Fig. S6.** ORR polarization curves of (a) Co@G/C<sub>ASP</sub>, (b) Co@G/C<sub>500</sub>, (c) Co@G/C<sub>600</sub> and (d) Co@G/C<sub>700</sub> in 0.1 M KOH before and after ADTs. For ORRs, scan rate: 5 mV s<sup>-1</sup>, rotation rate: 1600 rpm.

### Koutecky-Levich plots

To study the ORR kinetics followed by Co@G/C\_600 in 0.1 M KOH, Koutecky-Levich plots ( $J^1$  vs  $\omega^{-1/2}$ ) as shown in Fig. S7 were derived from rotation disk electrode measurements at different potentials. Here, the diffusion-limiting current increased with increasing rotation rate because of enhanced mass transfer of O<sub>2</sub> molecules. Besides, the great linearity and near-parallelism of the fitting lines of the K-L plots show clearly first order reaction kinetics with respect to the O<sub>2</sub> concentration. Their slopes also remained almost constant over the potential range of 0.40–0.60 V which implies almost similar electron transfer number at different potentials. The calculated electron transfer number,  $n$ , for Co@G/C\_600 is 3.6 which implies the ORR at catalyst in alkaline media primarily undergoes a 4e<sup>-</sup> pathway.

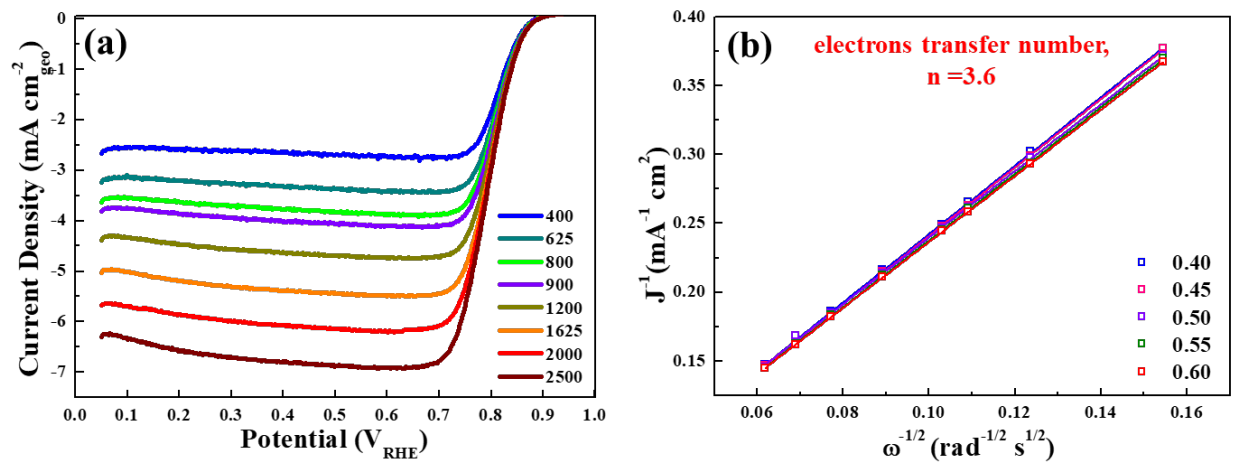


**Fig. S7.** (a) Co@G/C\_600 in O<sub>2</sub> saturated 0.1 M KOH solution at a scanning rate of 100 mV s<sup>-1</sup> at various rotation rates ranging from 400 to 2500 rpm, (b) their Koutecky-Levich plots at different potentials.

## Computational Methodology

Spin-polarized density functional theory calculations were performed using the Vienna *ab initio* Simulation Package (VASP)<sup>18-21</sup> with the projector-augmented wave (PAW)<sup>22,23</sup> method. Electron exchange-correlation functionals were represented with the generalized gradient approximation (GGA), and the model of Perdew, Burke and Ernzerhof (PBE)<sup>24</sup> was used for the nonlocal corrections. A kinetic energy cutoff of 400 eV was used with a plane-wave basis set. The Brillouin zone integrations for the bulk cobalt (Co) and graphene coated on Co substrate (Co@G) were conducted using a  $2 \times 2 \times 1$  Monkhorst-Pack grid<sup>25</sup> with the first-order Methfessel-Paxton smearing<sup>26</sup> with a width of 0.1 eV. The geometries were optimized until the total energy change upon two steps of the electronic self-consistent less than  $10^{-4}$  eV and the ionic relaxation loop smaller than  $10^{-3}$  eV. The dipole interactions were corrected for the total energy by using LDIPOL = .TRUE. and IDIPOL = 3 in VASP.

An orthorhombic supercell of  $13.15 \times 9.94 \times 24$  Å with periodic boundary conditions was designed for the Co@G surface system (5 layers). The vacuum space for the systems was larger than 16 Å. The Co(001)-*p*(6 × 4) surface consisted of a four-layer slab which had the two bottom layers fixed at the lattice constant of  $a = 2.484$  Å and  $c = 4.037$  Å (experimental values<sup>27</sup> are  $a = 2.507$  Å and  $c = 4.069$  Å). Based on this, the Co@G surface was modelled by adsorbing a graphene sheet that consisted of 48 carbon atoms on the top of Co(001) surface as described in Fig. S8. The optimization of graphene and N-doped graphene was performed under the same conditions of the Co@G surface system. N-doping graphene systems were mimicked by replacing the carbon atoms of graphene with nitrogen atoms depending on the number of N atoms and the N-doping sites.

The work function ( $\Phi$ ), which is minimum energy to remove an electron from a surface to a vacuum space (outside a surface), is defined as  $\Phi = E_{vacuum} - E_{Fermi}$ , where  $E_{vacuum}$  and  $E_{Fermi}$  are the potential in the vacuum (outside a surface) and the Fermi energy of the material, respectively. The calculated work function values of free standing graphene (G), graphene coated on Co substrate (Co@G), and N-doped graphene ( $N_xG$ ) (x represents number of doped N atoms) are quoted in Table S1. Since the lower work function values indicate the higher electron transfer, these results imply that the Co@G and N-doped graphene may have a higher interaction between adsorbate and surface

The adsorption energy ( $E_{ads}$ ) is defined as  $E_{ads} = E_{substrate+adsorbate} - E_{substrate} - E_{adsorbate}$ , where  $E_{substrate+adsorbate}$ ,  $E_{substrate}$ , and  $E_{adsorbate}$  are the total energies of an adsorption system (e.g., Co@G with adsorbed O), a substrate (Co@G), and a gas phase

adsorbate (O), respectively. A negative adsorption energy indicates that an adsorbate is strongly adsorbed on a substrate. To facilitate the search of the most stable adsorption site, we conducted preliminary adsorption energy calculations of  $\text{CN}^-$  without dipole correction at the various adsorption sites of  $\text{CoO}(100)$ ,  $\text{Co}_3\text{O}_4(110)$ ,  $\text{Co}_3\text{O}_4(111)$ , and  $\text{Pt}(111)$  surfaces.

The percentage of sites ( $N_{ads}$ ) corresponding to ORR efficiency is defined as  $N_{ads} = n_{ads}/n_{total}$ , where  $n_{ads}$  and  $n_{total}$  are the number of adsorption sites suitable for ORR (e.g., 114 sites where O atom can be stably adsorbed at  $\text{Co@G}$ ) and the total number of adsorption sites (132 sites at  $\text{Co@G}$ ), respectively.

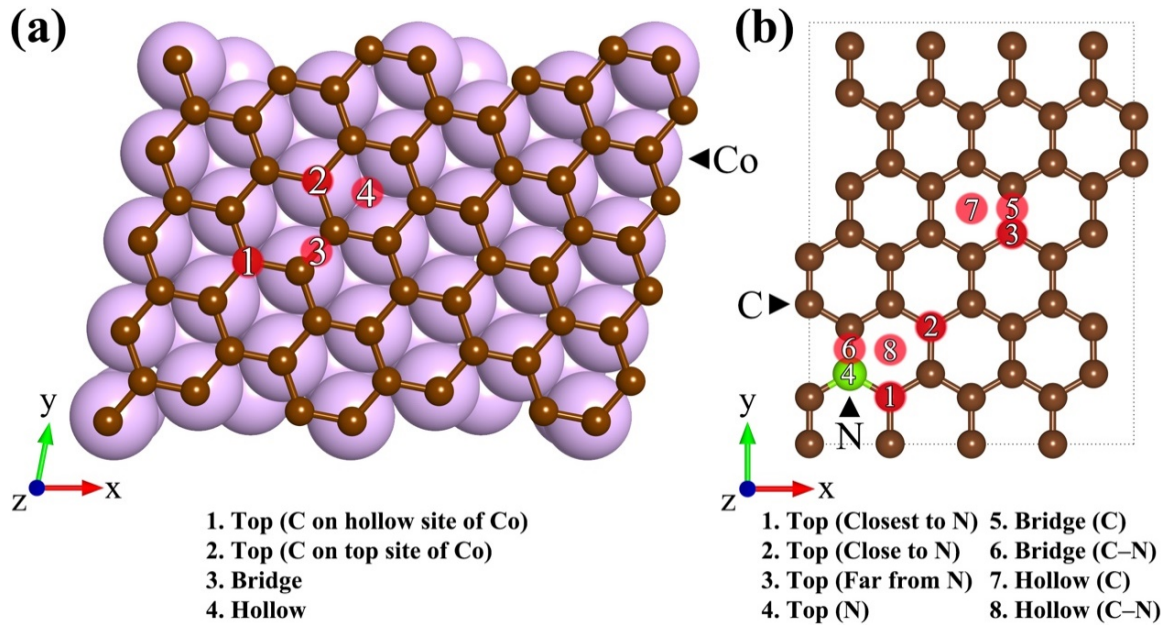


**Fig. S8.** (a) and (b) represent top views of  $\text{Co@G}$  system and  $\text{N}_1\text{G}$  system, respectively. Purple, small brown, and small lime spheres represent cobalt (Co), carbon (C), and nitrogen (N), respectively. Red circles indicate adsorption sites of O and  $\text{CN}^-$  at the  $\text{Co@G}$  system and those of O at the  $\text{N}_1\text{G}$  system. Detailed data are shown in Table S2 and S3.

**Table S1.** Work function of free standing graphene (G), N-doped graphene ( $N_xG$ , where x is the number of nitrogen), and graphene coated on Co (Co@G).

Surface System	Work Function (eV)	N-doping (%)
G	4.46	—
Co@G	3.18	—
$N_1G$	3.19	2.08
$N_3G$	2.91	6.25
$N_5G$	2.84	10.42

**Table S2.** Adsorption energies ( $E_{ads}$ ) of O depending on the adsorption sites at Co@G and  $N_1G$  systems. A superscript (1 ~ 8) represents adsorption sites as shown in Fig S8.

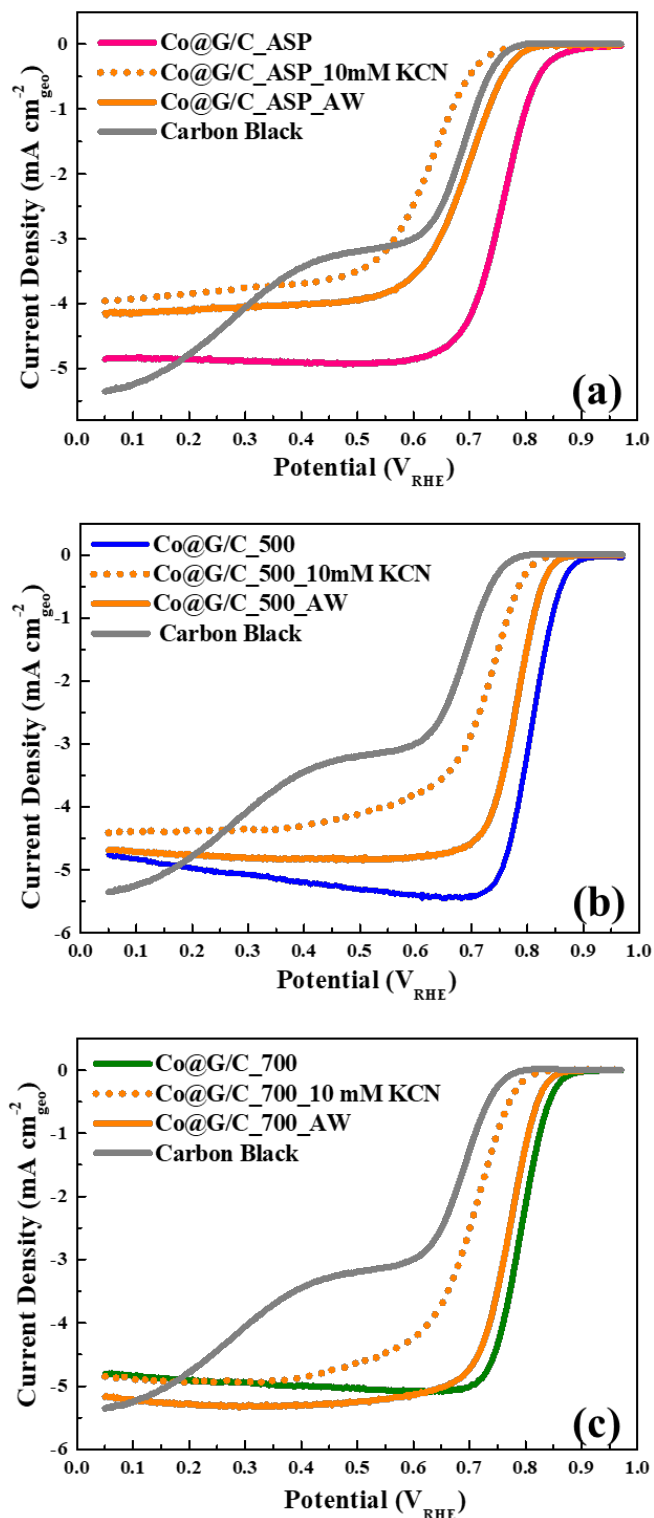
Adsorption sites	$E_{ads}$ (eV)	
	Co@G	$N_1G$
Top	-3.57 <sup>(1)</sup>	-3.21 <sup>(1)</sup>
		-2.55 <sup>(2)</sup>
	-3.27 <sup>(2)</sup>	-2.21 <sup>(3)</sup>
		-1.38 <sup>(4)</sup>
Bridge	-3.11 <sup>(3)</sup>	-2.51 <sup>(5)</sup>
		-3.19 <sup>(6)</sup>
Hollow	-1.10 <sup>(4)</sup>	-0.91 <sup>(7)</sup>
		-3.06 <sup>(8)</sup>

**Table S3.** Adsorption energies ( $E_{\text{ads}}$ ) of  $\text{CN}^-$  depending on adsorption sites at Co@G system.

A superscript (1 ~ 4) represents adsorption sites shown in Fig S8.

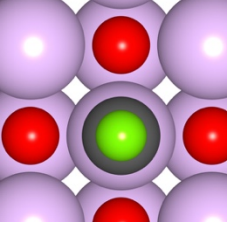
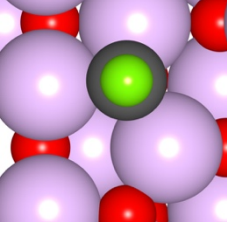
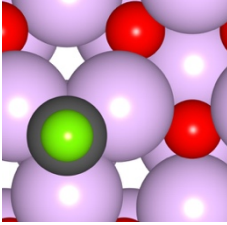
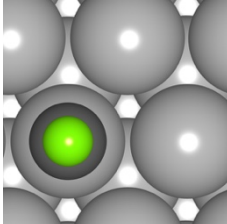
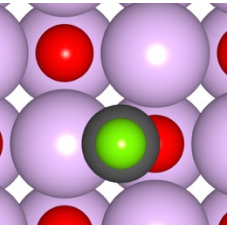
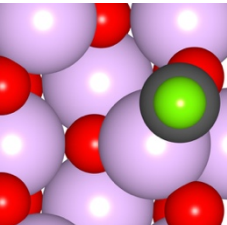
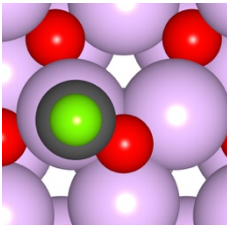
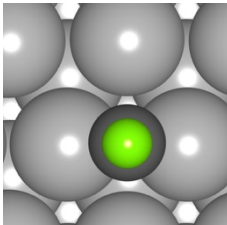
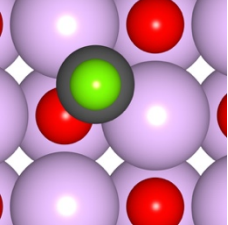
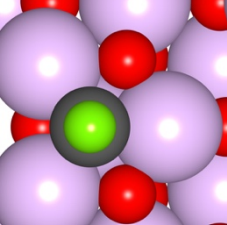
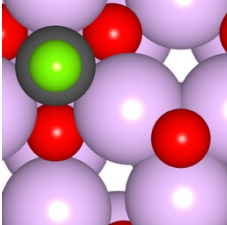
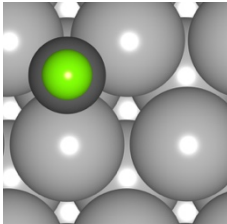
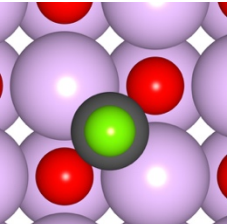
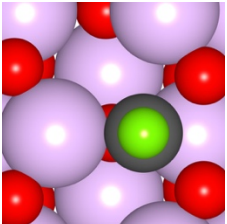
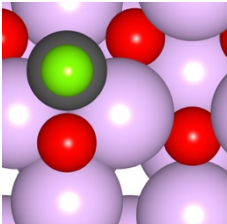
Adsorption sites	$E_{\text{ads}}$ (eV)
Top	-2.673 <sup>(1)</sup>
	-2.156 <sup>(2)</sup>
Bridge	-2.670 <sup>(3)</sup>
Hollow	-2.670 <sup>(4)</sup>

**SI 3. KCN poisoning/recovery tests:**



**Fig. S9.** ORR polarization curves of (a)  $\text{Co}@\text{G/C}_\text{ASP}$ , (b)  $\text{Co}@\text{G/C}_\text{500}$  and (c)  $\text{Co}@\text{G/C}_\text{700}$  in 0.1 M KOH with 10 mM KCN and after wash (AW) in fresh 0.1 M KOH electrolyte.

**Table S4.** Adsorbed configurations and adsorption energies ( $E_{\text{ads}}$ ) of  $\text{CN}^-$  at each site on the  $\text{CoO}(100)$ ,  $\text{Co}_3\text{O}_4(110)$ ,  $\text{Co}_3\text{O}_4(111)$ , and  $\text{Pt}(111)$  surfaces determined by preliminary DFT calculations without dipole correction. The adsorption energy in bold represents the most stable adsorption configuration used for the calculations shown in Fig. S10.

Adsorption sites	$E_{\text{ads}}$ (eV)			
	$\text{CoO}(100)$	$\text{Co}_3\text{O}_4(110)$	$\text{Co}_3\text{O}_4(111)$	$\text{Pt}(111)$
Top				
	-3.37	-1.78	-1.59	<b>-3.56</b>
Bridge				
	-2.47	-2.21	<b>-2.96</b>	-3.49
Hollow				
	<b>-3.94</b>	<b>-3.53</b>	-2.53	-3.48
				
	-2.88	-3.07	-2.85	

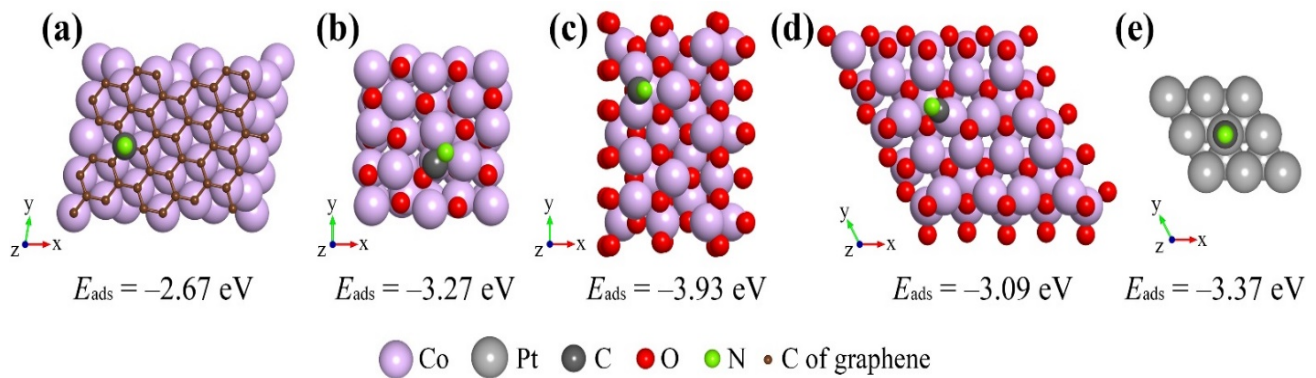


**Fig. S10.** Adsorption energies ( $E_{\text{ads}}$ ) of  $\text{CN}^-$  on different surfaces: **(a)** Co-graphene system (Co@G), **(b)** CoO (100), **(c)** Co<sub>3</sub>O<sub>4</sub> (110), **(d)** Co<sub>3</sub>O<sub>4</sub> (111) and **(e)** Pt (111)

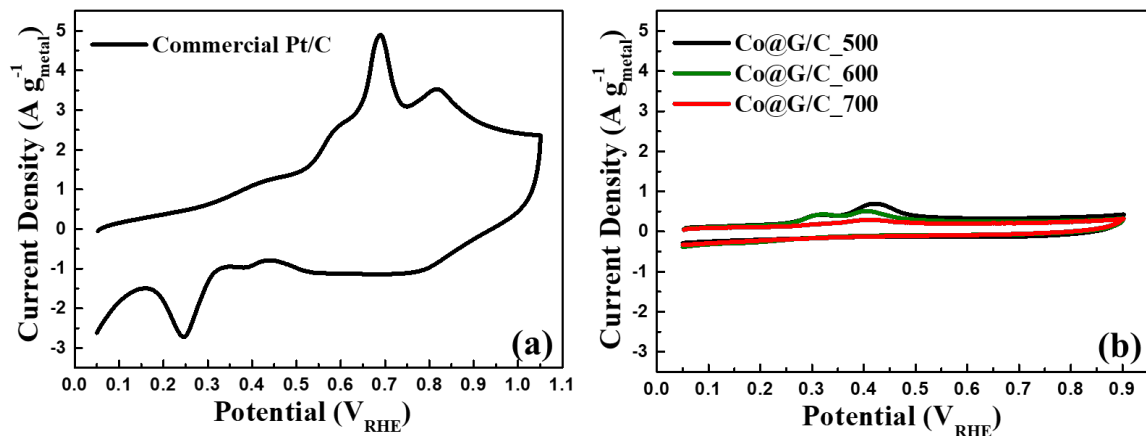


**Fig. S11.** CO stripping profile in 0.1 M KOH for (a) commercial Pt/C (20 wt.%) and (b) heat-treated Co@G/C samples.

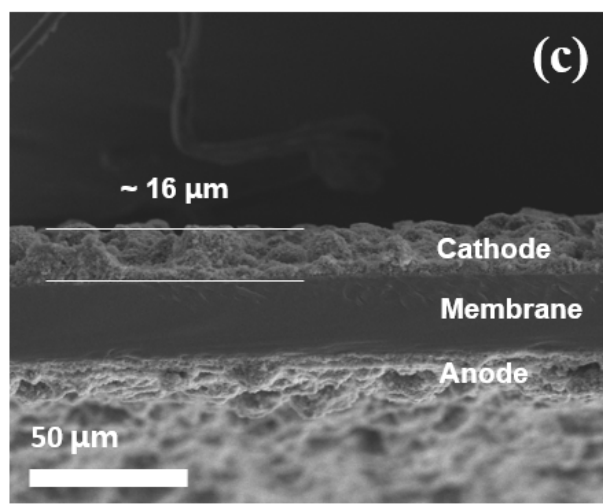
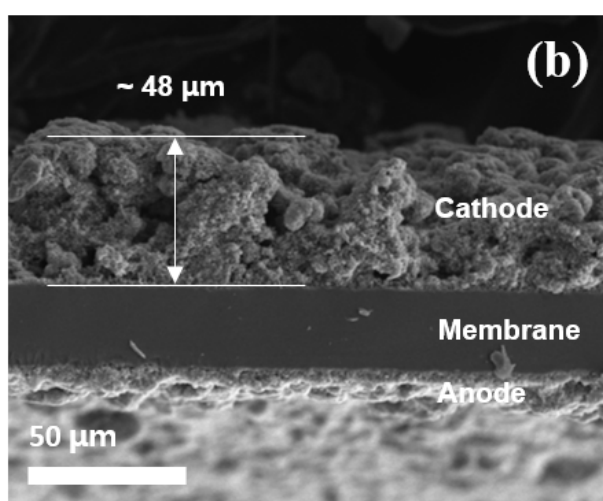
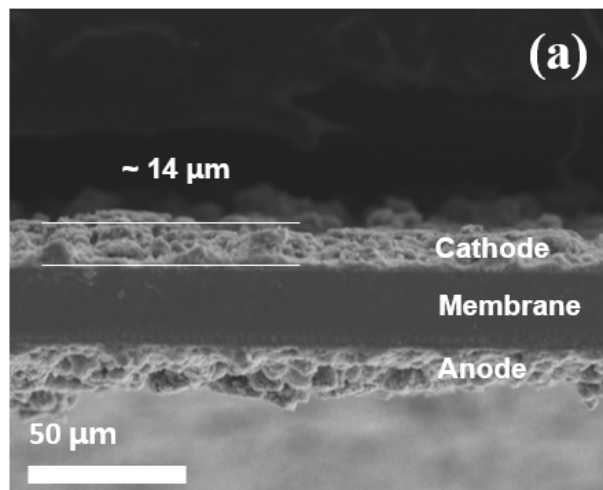


**Fig. S12.** Cross sectional SEM images of MEAs using (a) commercial Pt/C (46.5 wt% Pt, TKK), (b) Co@G/C (20 wt% Co), and (c) Co@G/C (40 wt% Co) in cathodes.

**Table S5.** Comparative study of components and performance of literature reported AEMFC.

Year	Cathode catalyst	Max power density (mW cm <sup>-2</sup> )	Catalyst loading (mg cm <sup>-2</sup> )	Membrane	Ionomer	Ref.
2011	Pt/C	196	0.4	Commercial (Tokuyama, A201)	Commercial (Tokuyama, AS-4)	28
	CoFeN/C	177	4	Commercial (Tokuyama, A201)	Commercial (Tokuyama, AS-4)	28
	NWNT/PyPBI/Pt	256	0.45	Commercial (Tokuyama, A201)	Commercial (Tokuyama, AS-4)	29
2012	Pt/C	62	0.5	Commercial (Fumatech, FAA)	Commercial (Fumatech, FAA)	30
	N-CNT	37	5	Commercial (Fumatech, FAA)	Commercial (Fumatech, FAA)	30
	Pt/C	120	0.6	Commercial (Tokuyama, A201)	Commercial (Tokuyama, AS-4)	31
	FePc/MWCNT	60	0.6	Commercial (Tokuyama, A201)	Commercial (Tokuyama, AS-4)	31
	CoPc/MWCNT	100	0.6	Commercial (Tokuyama, A201)	Commercial (Tokuyama, AS-4)	31
	Ag/C	109	0.5	Developed AEM (APSEBS AEM)	Developed AEI (QPSEBS AEI)	32
2013	Pt/C	223	0.8	Commercial (Fumatech, FAA-3)	Commercial (Fumatech, FAA-3)	33
	Pt/C	387	0.75	Commercial (Tokuyama, A201)	Commercial (Tokuyama, AS-4)	34
	CoO/rGO(N)	248	0.75	Commercial (Tokuyama, A201)	Commercial (Tokuyama, AS-4)	34
	Ag/C	190	1	Commercial (Tokuyama, A201)	Commercial (Tokuyama, AS-4)	35
	Pt/C	247	0.5	Commercial (Tokuyama, A201)	Commercial (Tokuyama, AS-4)	35
2014	Pt/C	520	0.5	Developed AEM	Commercial (Acta S.p.A., I2)	36
	CNT/HDC	221	2	Developed AEM	Commercial (Acta S.p.A., I2)	36
	Pt/C	407	0.4	Commercial (Tokuyama, A201)	Commercial (Tokuyama, AS-4)	37
	Ag/CNT	26	0.5	Commercial (Fumatech, FAA membrane)	Developed AEI (following the work of Arges et al.)	38
	AP-CoPc/C	21.7	1.5	Commercial (Tokuyama, A201)	Commercial (Tokuyama, AS-4)	39
2015	Pt/C	80	0.5	Commercial (Tokuyama, A201)	Commercial (Tokuyama, AS-4)	40

	Fe-N-C	75	4	Commercial (Tokuyama, A201)	Commercial (Tokuyama, AS-4)	40
	Co-N-C	68	4	Commercial (Tokuyama, A201)	Commercial (Tokuyama, AS-4)	40
	AgNW	164	1.05	Commercial (Tokuyama, A901)	Developed AEI (home-made AEI)	41
	Pt/C	737	0.4	Commercial (Tokuyama, A901)	Commercial (Tokuyama, AS-4)	42
2016	N-S-MPC	21	3	Commercial (Tokuyama, A201)	Commercial (Tokuyama, AS-4)	43
	Pt/C	120	0.6	Commercial (Tokuyama, A201)	Commercial (Tokuyama, AS-4)	44
	Co/N/MWCNT	110	0.6	Commercial (Tokuyama, A201)	Commercial (Tokuyama, AS-4)	44
	Pt/C	800	0.4	Developed AEM (PVB-MPY AEM) -Varcoe group-	Developed AEI (QAPS based AEI) -Varcoe group-	45
2017	Co9S8/G-500	31	2	Commercial (ASTOM, AHA-NEOSEPTA)	Commercial (Fumatech, Fumion FAA-3)	46
	BIDC(FeNC)	42	4	Commercial (Tokuyama, A201)	Commercial (Tokuyama, AS-4)	47
	Pt/C	1160	0.4	Developed AEM (ETFE-based AEM) -Varcoe group-	Developed AEI (ETFE-based AEI) -Varcoe group-	48
	Pt/C	1450	0.4	Developed AEM (LDPE-AEM) -Varcoe group-	Developed AEI (ETFE-based AEI) -Varcoe group-	49
	Ag/C	900	0.8	Commercial	Commercial	49
2018	Pt/C	330	0.2	Commercial (Tokuyama, A201)	Commercial (Tokuyama, AS-4)	50
	Fe/N/CDC	80	1.5	Commercial (Tokuyama, A201)	Commercial (Tokuyama, AS-4)	51
	Fe-NMG	218	3.5	Commercial (Tokuyama, A201)	Commercial (Tokuyama, AS-4)	52
	Non-PGM(carbon)	169	2	Commercial	Commercial	53
	Pt/C	1900	0.6	Developed AEM (ETFE-based AEM) -Varcoe group-	Developed AEI (ETFE-based AEI) -Varcoe group-	54
	Co@G/C_600	412	0.4	Commercial (Tokuyama, A201)	Commercial (Acta S.p.A., I2)	This work

## REFERENCES:

1. J. Wang, Z. Wu, L. Han, R. Lin, H. L. Xin and D. Wang, *ChemCatChem*, 2016, **8**, 736–742.
2. J. X. Wang, C. Ma, Y. Choi, D. Su, Y. Zhu, P. Liu, R. Si, M. B. Vukmirovic, Y. Zhang and R. R. Adzic, *J. Am. Chem. Soc.*, 2010, **133**, 13551–13557
3. K. Borogohain, J. B. Singh, M. V. Rama Rao, T. Shripathi and S. Mahamuni, *Phys. Rev. B* 2000, **61**, 11093–11096.
4. Jade X-ray database, Release 5.022, 2000 (ICDD).
5. G. P. Glaspey, P. W. Jagodzinski and A. Manivannan, *J. Phys. Chem. B* 2004, **108**, 9604–9607.
6. J. Liu, L. Jiang, B. Zhang, J. Jin, D. S. Su, S. Wang and G. Sun, *ACS Catal.* 2014, **4**, 2998–3001.
7. N. Patel, A. Santini, V. Bello, G. Matteia and A. Miotello, *Surf. Coat. Technol.*, 2013, **235**, 784–791.
8. R. Edla, S. Gupta, N. Patel, N. Bazzanella, R. Fernandes, D.C. Kothari and A. Miotelloa, *Appl. Catal. A: Gen.*, 2016, **515**, 1–9.
9. L. Zhuo, Y. Wu, J. Ming, L. Wang, Y. Yu, X. Zhang and F. J. Zhao, *J. Mater. Chem. A*, 2013, **1**, 1141–1147.
10. P. Cai, S. Ci, E. Zhang, P. Shao, C. Cao and Z. Wen, *Electrochim. Acta*, 2016, **220**, 354–362.
11. X. Liu, R. Yi, Y. Wang, G. Qiu, N. Zhang and X. Li, *J. Phys. Chem. C*, 2007, **111**, 163–167.
12. S. P. Gubin, Y. I. Spichkin, Y. A. Koksharov, G. Y. Yurkov, A. V. Kozinkin, T. I. Nedoseikina, M. S. Korobov and A. M. Tishin, *J. Magn. Magn. Mater.*, 2003, **265**, 234–242.

13. N. A. M. Barakat, M. El-Newehy, S. S. Al-Deyab and H. Y. Kim, *Nanoscale Res. Lett.*, 2014, **9**, 2-10.
14. Y. Z. Chen, C. Wang, Z. Y. Wu, Y. Xiong, Q. Xu, S. H. Yu and H. L. Jiang, *Adv. Mater.*, 2015, **27**, 5010-5016.
15. Z.-Y. Wu, P. Chen, Q. S. Wu, L. F. Yang, Z. Pan and Q. Wang, *Nano Energy*, 2014, **8**, 118-125.
16. V. Vij, J. N. Tiwari and K. S. Kim, *ACS Appl. Mater. Interfaces*, 2016, **8**, 16045–16052.
17. M. Shen, L. Zheng, W. He, C. Ruan, C. Jiang, K. Ai and L. Lu, *Nano Energy*, 2015, **17**, 120–130.
18. G. Kresse and J. Hafner, *Phys. Rev. B*, 1993, **47**, 558-561.
19. G. Kresse and J. Hafner, *Phys. Rev. B*, 1994, **49**, 14251-14269.
20. G. Kresse and J. Furthmüller, *Phys. Rev. B*, 1996, **54**, 11169-11186.
21. G. Kresse and J. Furthmüller, *Comput. Mater. Sci.*, 1996, **6**, 15-50.
22. P. E. Blöchl, *Phys. Rev. B*, 1994, **50**, 17953-17979.
23. G. Kresse and D. Joubert, *Phys. Rev. B*, 1999, **59**, 1758-1775.
24. J. P. Perdew, K. Burke and M. Ernzerhof, *Phys. Rev. Lett.*, 1996, **77**, 3865-3868.
25. H. J. Monkhorst and J. D. Pack, *Phys. Rev. B*, 1976, **13**, 5188-5192.
26. M. Methfessel and A. T. Paxton, *Phys. Rev. B*, 1989, **40**, 3616-3621.
27. X. Li, B. N. Popov, T. Kawahara and H. Yanagi, *J. Power Sources*, 2011, **196**, 1717-1722.
28. M. J. Mehl and D. A. Papaconstantopoulos, *Phys. Rev. B*, 1996, **54**, 4519-4530.
29. K. Matsumoto, T. Fujigaya, H. Yanagi and N. Nakashima, *Adv. Funct. Mater.*, 2011, **21**, 1089-1094.
30. C. V. Rao and Y. Ishikawa, *J. Phys. Chem. C*, 2012, **116**, 4340-4346.
31. R. Vinodh and D. Sangeetha, *J. Mater. Sci.*, 2012, **47**, 852-859.
32. I. Kruusenberg, L. Matisen, Q. Shah, A. M. Kannan and K. Tammeveski, *Int. J. Hydrogen*

- Energy*, 2012, **37**, 4406-4412.
33. M. Carmo, G. Doubek, R. C. Sekol, M. Linardi and A. D. Taylor, *J. Power Sources*, 2013, **230**, 169-175.
34. Q. He, Q. Li, S. Khene, X. Ren, F. E. López-Suárez, D. Lozano-Castelló, A. Bueno- López and G. Wu, *J. Phys. Chem. C*, 2013, **117**, 8697-8707.
35. L. Xin, Z. Zhang, Z. Wang, J. Qi and W. Li, *Front. Chem.*, 2013, **1**, 16.
36. Y. J. Sa, C. Park, H. Y. Jeong, S. Park, Z. Lee, K. T. Kim, G. Park and S. H. Joo, *Angew. Chemie – Int. Ed.*, 2014, **126**, 4186-4190.
37. D. Yang, H. Yu, G. Li, Y. Zhao, Y. Liu, C. Zhang, W. Song and Z. Shao, *J. Power Sources*, 2014, **267**, 39-7.
38. A. Fazil and R. Chetty, *Electroanalysis*, 2014, **26**, 2380-2387.
39. M. Xu, C. Li, H. Ren, L. Ding, K. Xu and J. Geng, *J. Mol. Catal. A Chem.*, 2014, **390**, 69-75.
40. J. Sanetuntikul and S. Shanmugam, *Nanoscale*, 2015, **7**, 7644-7650.
41. L. Zeng, T. S. Zhao, and L. An, *J. Mater. Chem. A*, 2015, **3**, 1410-1416.
42. R. B. Kaspar, M. P. Letterio, J. A. Wittkopf, K. Gong, S. Gu and Y. Yan, *J. Electrochem. Soc.*, 2015, **162**, F483-488.
43. N. Xu, T. Zhu, J. Qiao, F. Zhang and Z. Chen, *Int. J. Hydrogen Energy*, 2016, **41**, 9159-9166.
44. I. Kruusenberg, D. Ramani, S. Ratso, U. Joost, R. Saar, P. Rauwel, A. M. Kannan and K. Tammeveski, *ChemElectroChem*, 2016, **3**, 1455-1465.
45. J. Ponce-González, D. K. Whelligan, L. Wang, R. Bance-Soualhi, Y. Wang, Y. Peng, H. Peng, D. C. Apperley, H. N. Sarode, T. P. Pandey, A. G. Divekar, S. Seifert, A. M. Herring, L. Zhuang and J. R. Varcoe, *Energy Environ. Sci.*, 2016, **9**, 3724-3735.
46. A. Arunchander, S. G. Peera, V. V. Giridhar and A. K. Sahu, *J. Electrochem. Soc.*, 2017,

**164**, F71-80.

47. R. Gokhale, Y. Chen, A. Serov, K. Artyushkova and P. Atanassov, *Electrochim. Acta*, 2017, **224**, 49-55.
48. L. Wang, E. Magliocca, E. L. Cunningham, W. E. Mustain, S. D. Poynton, R. Escudero-Cid, M. M. Nasef, J. Ponce-González, R. Bance-Souahli, R. C. T. Slade, D. K. Whelligan and J. R. Varcoe, *Green Chem.*, 2017, **19**, 831-843.
49. L. Wang, J. J. Brink, Y. Liu, A. M. Herring, J. Ponce-González, D. K. Whelligan and J. R. Varcoe, *Energy Environ. Sci.*, 2017, **10**, 2154-2167.
50. T. Reshetenko, M. Odgaard, D. Schlueter and A. Serov, *J. Power Sources*, 2018, **375**, 185-190.
51. S. Ratso, I. Kruusenberg, M. Käärik, M. Kook, L. Puust, R. Saar, J. Leis and K. Tammeveski, *J. Power Sources*, 2018, **375**, 233-243.
52. M. M. Hossen, K. Artyushkova, P. Atanassov and A. Serov, *J. Power Sources*, 2018, **375**, 214-221.
53. M. J. Kim, O. Kim, S. Kim, Y. Choi, Y. Cho and Y. Sung, *J. Ind. Eng. Chem.*, 2018, **61**, 437-444.
54. T. J. Omasta, A. M. Park, J. M. Lamanna, Y. Zhang, X. Peng, L. Wang, D. L. Jacobson, J. R. Varcoe, D. S. Hussey, B. S. Pivovar and W. E. Mustain, *Energy Environ. Sci.*, 2018, **11**, 551-558.